Available online at www.sciencedirect.com
ScienceDirect
Trans. Nonferrous Met. Soc. China 34(2024) 3599−3614
Transactions of Nonferrous Metals Society of China
www.tnmsc.cn

Effects of ⟨*c*+*a*⟩ slip mode on microstructure evolution and compressive flow behavior of extruded dilute Mg−0.5Bi−0.5Sn−0.5Mn alloy

Zhi-yong YOU[1], Wei-li CHENG[1,2], Guo-lei LIU[1], Jian LI[2],
Li-fei WANG[1], Hui YU[3], Hong-xia WANG[1], Ze-qin CUI[1], Jin-hui WANG[2]

1. School of Materials Science and Engineering, Taiyuan University of Technology, Taiyuan 030024, China;
2. Salt Lake Chemical Engineering Research Complex, Qinghai University, Xining 810016, China;
3. School of Materials Science and Engineering, Hebei University of Technology, Tianjin 300132, China

Received 29 December 2023; accepted 30 July 2024

Abstract: The influence of the slip mode on the microstructure evolution and compressive flow behavior at different strains in an extruded dilute Mg−0.5Bi−0.5Sn−0.5Mn alloy was analyzed through electron backscatter diffraction, X-ray diffraction, transmission electron microscopy, and hot compression tests. The results showed that at a low strain of 0.05, the basal ⟨*a*⟩, pyramidal ⟨*a*⟩ and ⟨*c*+*a*⟩ slip modes were simultaneously activated. Nevertheless, at the middle stage of deformation (strain of 0.1, 0.2 and 0.5), the ⟨*a*⟩ slip mode was difficult to be activated and ⟨*c*+*a*⟩ slip mode became dominant. The deformation process between strains of 0.2 and 0.5 was primarily characterized by the softening effect resulting from the simultaneous occurrence of continuous dynamic recrystallization and discontinuous dynamic recrystallization. Ultimately, at strain of 0.8, a dynamic equilibrium was established, with the flow stress remaining constant due to the interplay between the dynamic softening brought about by discontinuous dynamic recrystallization and the work-hardening effect induced by the activation of the basal ⟨*a*⟩ slip mode.
Key words: dilute Mg−Bi−Sn−Mn alloy; slip mode; hot compression; flow behavior; dynamic recrystallization

1 Introduction

Magnesium (Mg) and its alloys have advantages of low density and excellent castability. But the wide application of Mg is restricted owing to its intrinsic limitations of poor strength-ductility synergy and formability, which have a close correlation with the activation of basal slip and the strong basal texture [1,2]. Therefore, increasing the activity of non-basal slip and twinning is an effective strategy to improve the strength and formability of Mg alloys at relatively low temperature [3,4].

SHEN et al [5] reported that activation of the slip mode was closely related to the critical resolved shear stress (CRSS) of the material. Alloying is an effective method to regulate $CRSS_{non\text{-}basal}/CRSS_{basal\langle a\rangle}$ ratio [6]. For example, CHAUDRY et al [7] reported that by lowering the ratio of CRSSs between non-basal slips and basal slip, AZ31-0.5Ca (wt.%) Mg alloy may effectively weaken basal texture and activate additional non-basal slip modes.

Dynamic recrystallization (DRX) is an important softening mechanism during compression process. Additionally, WU et al [8] examined the DRX behavior of ZM51 Mg alloys and discovered that an increment in strain rates will lead to an increment in DRX degree, which will weaken texture and refine grains.

Heterostructure consisting of typical bimodal

Corresponding author: Wei-li CHENG, Tel: +86-18636612588, E-mail: chengweili7@126.com
DOI: 10.1016/S1003-6326(24)66628-8

grain-sized grains usually has good deformation ability and excellent synergistic effect of strength and plasticity. Recent research suggested that the heterogeneous deformation in local domains is conducive to generate hetero-deformation induced (HDI) stress, thus providing additional strain hardening [9,10]. According to a recent study [11], the outstanding Schmid factor difference (SFD) between neighboring grains in the Mg−13Gd (wt.%) alloy can likewise generate HDI stress.

Based on our previous study, dilute Mg−Bi−Sn alloy inherently owes excellent deformation ability. For instance, LIU et al [12] reported that the Mg−0.25Bi−0.25Sn (wt.%) alloy has almost no unstable processing area under the different strains. Moreover, SOMEKAWA and SINGH [13] prepared a Mg−0.3Bi (at.%) alloy with low fraction of Mg_3Bi_2 phase, which exhibits excellent ductility during tension deformation. However, high alloying may generate phase particle, which brings about stress concentration and weakens the deformation ability of Mg alloys to some extent. Furthermore, at present, the effect of activity of slip modes on microstructure evolution and compressive flow behavior is still limit, and it still needs to be further revealed.

Therefore, the influence of activity of slip modes on microstructure evolution and compressive flow behavior at different strains in an extruded dilute Mg−0.5Bi−0.5Sn−0.5Mn alloy was deeply analyzed to offer guidelines for the development of wrought dilute Mg alloys with exceptional formability at low temperature and high strain rate.

2 Experimental

The as-cast Mg−0.5Bi−0.5Sn−0.5Mn (wt.%) alloy was prepared in an electric resistance furnace under a protective atmosphere (SF_6:CO_2=1:40, volume ratio) and was denoted as BTM000. The cast alloys were then subjected to solid-solution treatment in a muffle furnace at 320 °C for 1 h and 500 °C for 3 h prior to extrusion. The solid-solution-treated alloy underwent extrusion at a temperature of 225 °C, employing a 9:1 extrusion ratio and a 0.1 mm/s extrusion speed [14].

Cylindrical specimens were subjected to machining for the purpose of conducting hot compression experiments, utilizing a Gleeble−3500D thermal simulation apparatus. The compression experiments were tested at a temperature of 225 °C and a strain rate of 30 s^{-1}. Furthermore, in order to study the microstructure evolution, each test was tested at true strains of 0.05, 0.1, 0.2, 0.5 and 0.8, respectively. After testing, each sample was subjected to water quenching to preserve its high-temperature deformation structures.

X-ray diffraction (XRD, Rigaku Ultima IV) was used to determine the phase compositions. Transmission electron microscopy (TEM, JE−2100F) images revealed the particular microstructure morphology. The compressed samples were subjected to electron backscatter diffraction (EBSD, EDAX Hikari Plus) at step of 0.2 μm.

3 Results

3.1 Initial microstructure

Figure 1 shows the initial microstructure of the BTM000 alloy. As shown in Fig. 1(a), the alloy has a typical bimodal grain structure consisting of fine DRXed grains and elongated deformed grains. In addition, the average grain size is ~14.18 μm. Figures 1(b) and (c) show that the texture component is distributed along the arc between $[01\bar{1}0]$//ED and $[\bar{1}2\bar{1}0]$//ED, while the peak texture occurs along the arc between $[01\bar{1}0]$//ED and $[3\bar{1}\bar{2}0]$//ED, with a multiple random distribution (MRD) of 10.79.

As shown in Figs. 1(d, e), few particles can be observed in the local region, and the selected area electron diffraction (SAED) images confirm that the precipitates are Mg_3Bi_2 and α-Mn, respectively. However, the XRD pattern (Fig. 2) indicates that no precipitates except for the α-Mg phase are detected in the studied alloy. In this respect, the studied alloy could be determined to be a precipitate-free alloy.

3.2 True stress−strain curves

Figure 3 shows the true stress–strain curve of the BTM000 alloy compressed at 225 °C with a strain rate of 30 s^{-1}, which could be divided into four stages. At the Stage I, the flow stress increases linearly with increasing strain. Note that a sharply concave curvature (red dotted rectangle) could be observed during the subsequent deformation. During the Stage II, the slope of the flow stress decreased, indicating a decrease in the dislocation proliferation rate. At the Stage III, the flow stress

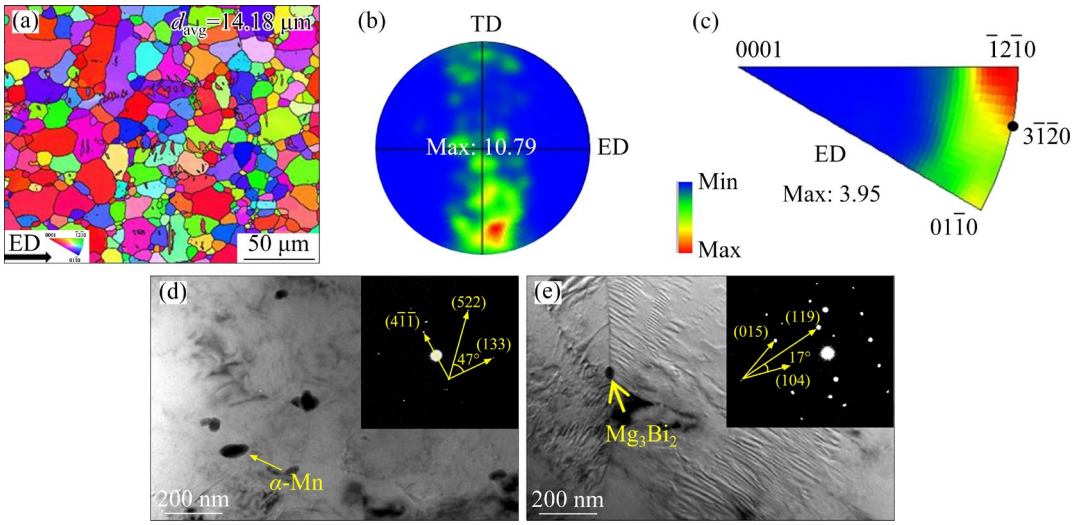

Fig. 1 Initial microstructure of BTM000 alloy: (a) IPF map; (b) (0001) pole figure; (c) ED IPF map; (d, e) TEM and SAED images of α-Mn and Mg_3Bi_2, respectively

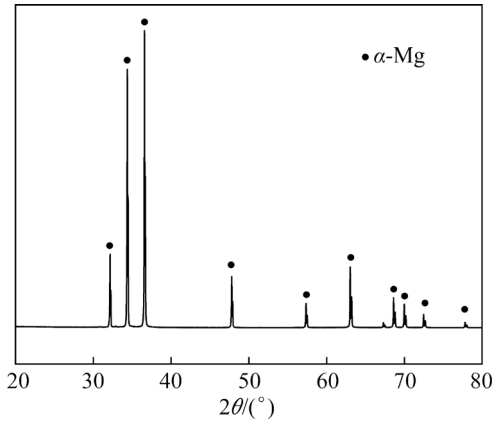

Fig. 2 XRD pattern of BTM000 alloy

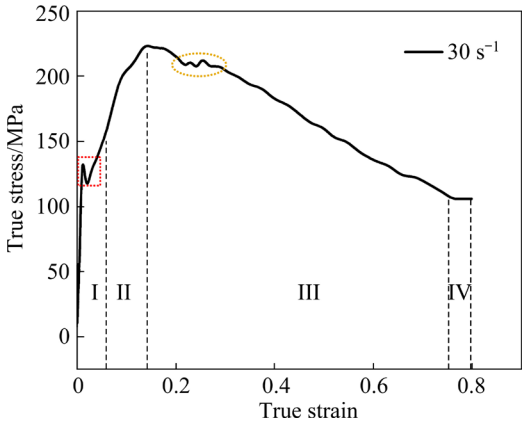

Fig. 3 True stress–strain curve of BTM000 alloy

continues to decrease from the peak, and the periodic similarity zigzag (yellow dotted ellipse) in the curve can also be observed. As the true strain increases to approximately 0.8 (Stage IV), the flow stress tends to reach dynamic equilibrium.

3.3 Microstructure evolution

Figure 4 shows the microstructural evolution of the studied alloy obtained at strains of 0.05, 0.1 0.2, 0.5 and 0.8. At the initial stage of deformation (Fig. 4(a)), numerous deformed grains can be observed, which is connected with the blocking effect of the original grain boundary (GB). Additionally, an examination of the respective GB map (Fig. 4(a_1)) and DRX map (Fig. 4(a_2)) confirms the presence of numerous twins dispersed within the interior of the deformed grain. The identification of twin types is facilitated through the analysis of misorientation angles and rotation axes. For instance, within the range of 80°−90°, a prominent $\langle 2\bar{1}\bar{1}0\rangle$ rotation axis is discernible (Fig. 4(f)), signifying the existence of $\{10\bar{1}2\}$ extension twinning (ETW). The criteria for identifying DRXed and unDRXed grains were partitioned on the basis of kernel average misorientation (KAM). Specifically, (1) software analysis system reconstructed grains' information based on the imported EBSD data; (2) then it collected each grain and measured the KAM within the grain; (3) the deformed grains were defined that the average misorientation in a grain exceeded the self-defined minimum misorientation threshold (θ_t=1°) that defined a subgrain [15]; (4) the case that some grains whose KAM was below θ_t but the misorientation between these grains was above θ_t were classified as subgrains; (5) the remaining grains were classified as DRXed grains. As a result, the DRXed grains, subgrains and deformed grains

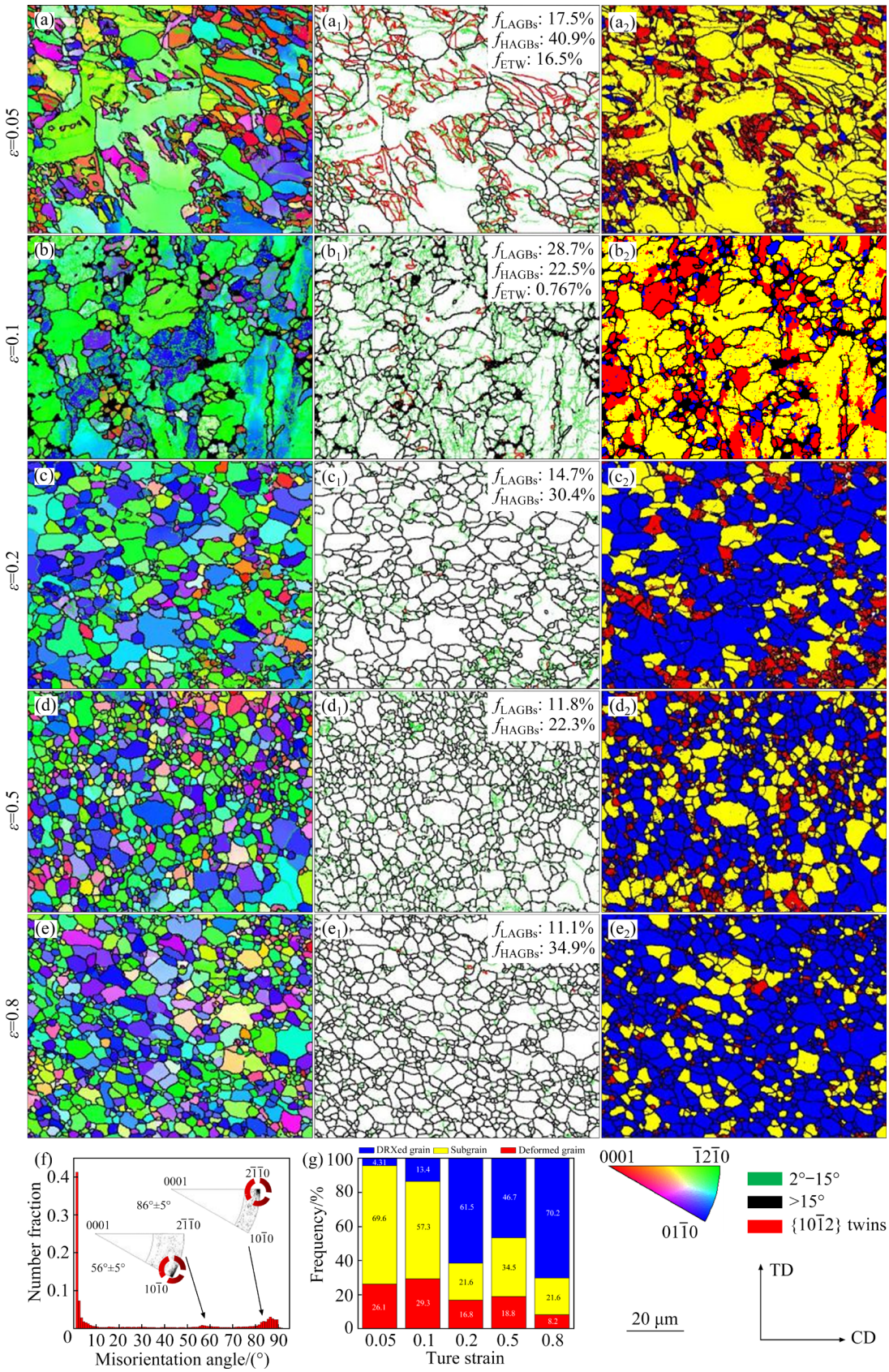

Fig. 4 Inverse pole figure (IPF) (a−e), GB (a_1−e_1) and DRX (a_2−e_2) maps of BTM000 alloy obtained after hot compression at different strains: (a−a_2) 0.05; (b−b_2) 0.1; (c−c_2) 0.2; (d−d_2) 0.5; (e−e_2) 0.8; (f) Misorientation angle distribution map and corresponding axis distribution at strain of 0.05; (g) Frequency of DRXed grain, subgrain and deformed grain

extracted from the overall grains were labelled as blue, yellow and red colors in Figs. 4(a_2−e_2). As the strain increases to 0.1, the merging and growth of subgrains indicate that dynamic recovery (DRV) occurs. In addition, the fraction of newly formed DRXed grains distributed along the GBs of the deformed grains increases to 13.4% (Fig. 4(g)), which is characteristic of the discontinuous dynamic recrystallization (DDRX) mechanism [16]. Note that the fraction of low-angle grain boundaries (LAGBs) increased from 17.5% to 28.7% due to the great decrease in the ETW. With a further increase in the strain to 0.2, a great number of LAGBs grow into high-angle grain boundaries (HAGBs) through rotation of subgrains and subsequently form DRXed grains, which is a characteristic of continuous dynamic recrystallization (CDRX) [17].

However, at a strain of 0.5, the fraction of DRXed grains decreases from 61.5% to 46.7%, which is ascribed to the fact that the activation of the ⟨*c*+*a*⟩ slip system facilitates DRX nucleation rather than grain growth. However, the fraction of DRXed grains increases to 70.2% at a strain of 0.8, indicating an increased DRX degree [18].

3.4 Texture evolution

Figures 5 and 6 show the texture component maps and {0001} pole figures (PFs), respectively.

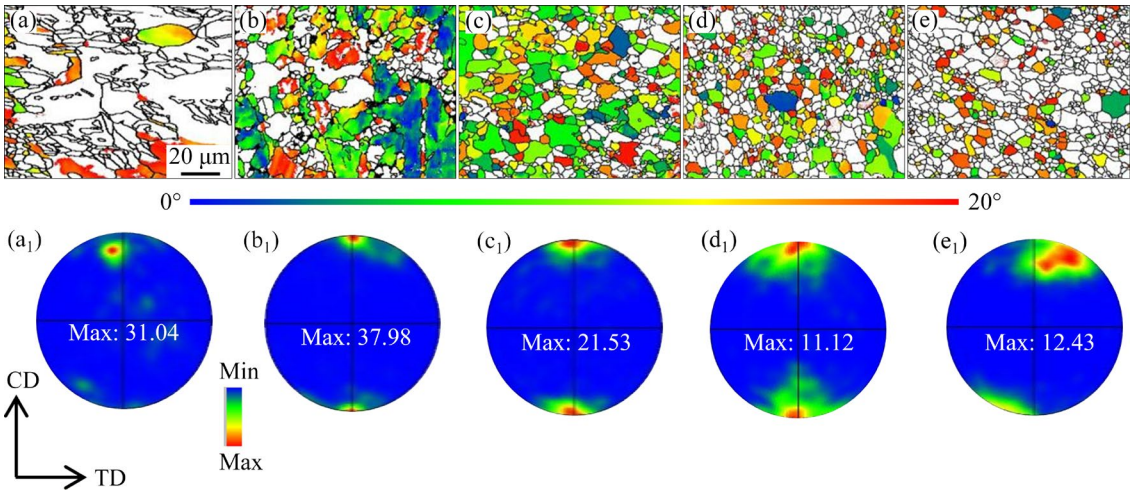

Fig. 5 Texture component maps (a−e) and corresponding (0001) PFs (a_1−e_1) of BTM000 alloy obtained after hot compression at different strains: (a, a_1) 0.05; (b, b_1) 0.1; (c, c_1) 0.2; (d, d_1) 0.5; (e, e_1) 0.8

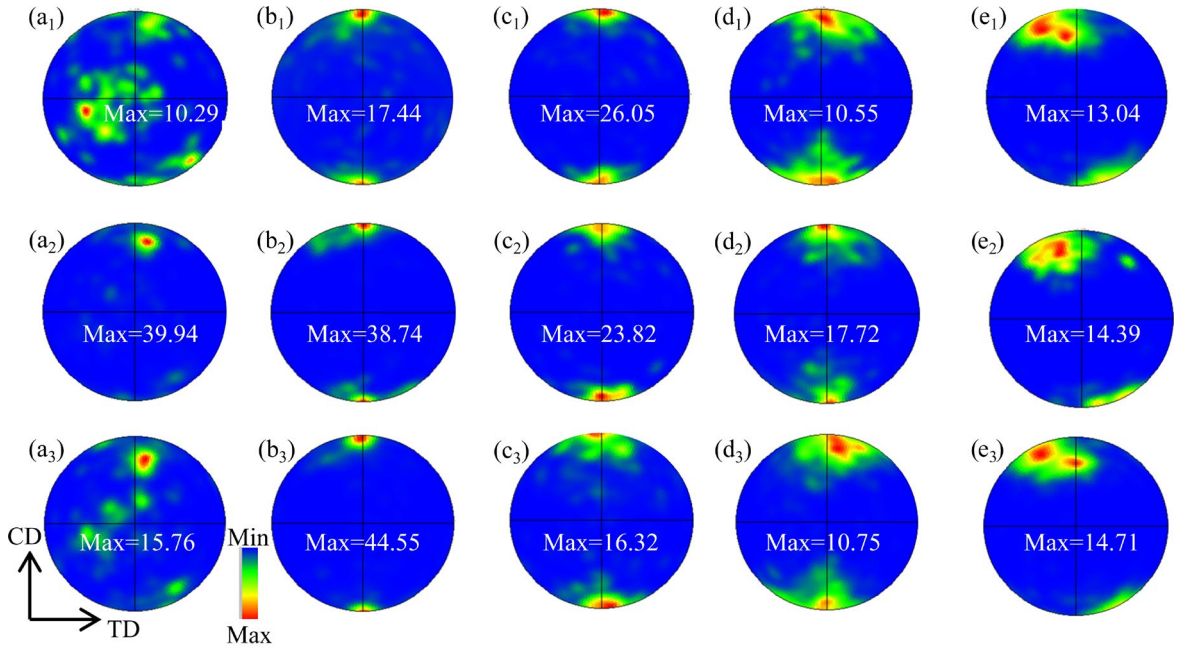

Fig. 6 PFs of BTM000 alloy obtained after hot compression at different strains: (a_1, a_2, a_3) 0.05; (b_1, b_2, b_3) 0.1; (c_1, c_2, c_3) 0.2; (d_1, d_2, d_3) 0.5; (e_1, e_2, e_3) 0.8; (a_1−e_1) DRXed grain; (a_2−e_2) Subgrain; (a_3−e_3) Deformed grain

The pole density points of all the samples are nearly concentrated on both sides of the compression direction (CD), which indicates that the texture type is a compression texture, i.e., ⟨0001⟩//CD. As shown in Figs. 5(a_1−e_1), the total texture intensity fluctuates irregularly with increasing strain. In addition, by comparing the DRX maps (Figs. 4(a_2−e_2)) with the texture component maps (Figs. 5(a−e)), the grains that dominate the micro-texture at different strains can be determined. The overall texture strength exhibits a rise from 31.04 MRD to 37.98 MRD, with an increase in strain from 0.05 to 0.1. This escalation can primarily be attributed to localized deformation disparities stemming from the absence of ETW. Similarly, with further increase in strain to 0.2 and 0.5, the deformed grains progressively undergo replacement by DRXed grains characterized by random orientations, resulting in a decrease in the total texture intensity to 21.53 MRD and 11.12 MRD, respectively. These findings align with the outcomes depicted in Figs. 6(b_3) and (c_1−d_1). Intriguingly, at a strain of 0.8, the total texture intensity experiences an upswing to 12.43 MRD in comparison to that observed at a strain of 0.5. This phenomenon may be attributed to the mechanisms governing DRX and the preferential growth of DRXed grains.

4 Discussion

4.1 Twinning behavior

Figure 7 shows the TEM images and high-magnification IPF maps after deformation at a strain of 0.05. As shown in Fig. 7(a), an obvious twin structure embedded into the Mg matrix could be observed. According to the corresponding SAED analysis, this sample is regarded as $\{10\bar{1}2\}$ ETW. Moreover, typical G1 and G2 grains were extracted from Fig. 4(a). Furthermore, local growth of the ETW could be observed, which is mostly ascribed to the widespread expansion of extension twin lamellae, and some extension twins with the same variant merged with each other [19]. In particular, in G2, the twin (T) component almost consumes the whole parent grain (P) (Fig. 7(d)). Interestingly, the misorientations among T1, T2 and T3 are (56°±5°), which could be attributed to the $\{10\bar{1}1\}$ compression twin. From Figs. 7(e) and (f), ETW presents more distinct texture components compared to those of the matrix; thus, the presence of ETW contributes to dispersing the texture intensity.

4.2 Slip modes

4.2.1 IGMA analysis

From the results of microstructure evolution and texture type, the presence of LAGBs and rotation of grains were observed, indicating that slip mode variation accompanied hot compression. Henceforth, an analysis of the in-grain misorientation axis (IGMA) was conducted to corroborate the slip modes at different strain levels. This analysis hinges on the presumption that the crystal lattice undergoes deformation due to slip along a specific Taylor axis, as detailed in Table 1, utilizing EBSD data [20].

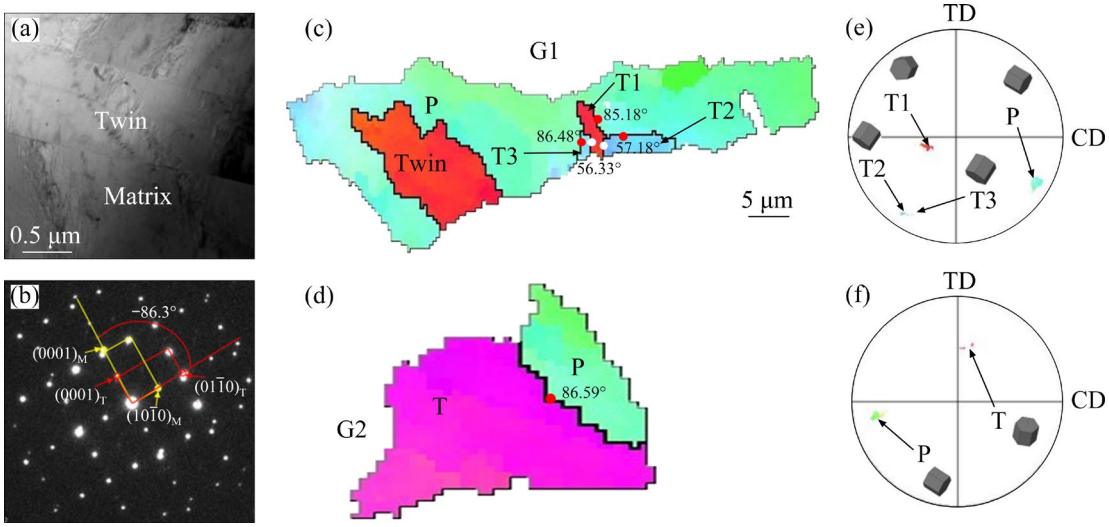

Fig. 7 (a) Bright field image; (b) Selected area electron diffraction pattern; (c, d) High-magnification IPF maps of G_1 and G_2, respectively; (e, f) PFs of G_1 and G_2, respectively

Table 1 Deformation mechanisms in Mg alloy and corresponding Taylor axes [20]

Slip plane	Slip direction	Taylor axis
{0001}	$\langle 11\bar{2}0\rangle$	$\langle 10\bar{1}0\rangle$
$\{10\bar{1}0\}$	$\langle 11\bar{2}0\rangle$	⟨0001⟩
$\{11\bar{2}2\}$	$\langle 11\bar{2}3\rangle$	$\langle 1\bar{1}00\rangle$
$\{10\bar{1}1\}$	$\langle 11\bar{2}0\rangle$	$\langle 10\bar{1}2\rangle$

The representative IGMA distributions developed in the BTM000 alloy at different strains with corresponding KAM maps are shown in Fig. 8. Given that the KAM map serves as an indicator of the localized deformation extent, it is noteworthy that the selected deformed grains, denoted by capital letters A−F in Figs. 8(a−e), also find representation in Figs. 8(a_1−e_1). These chosen grains exhibit elevated dislocation densities. According to Fig. 8(a_1), the IGMA distribution in Grain B is concentrated on the ⟨0001⟩ axis with maximum intensity (MI) higher than 2.0 MRD, which suggests that prismatic ⟨*a*⟩ slip predominates the deformation process. Note that the IGMA around the $\langle 10\bar{1}2\rangle$ axis is observed in Grain A, which indicates that pyramidal ⟨*a*⟩ slip is activated. Nevertheless, for the remaining grains with MIs greater than 2.0 MRD, the IGMA distribution matches the ⟨*uvt*0⟩ axis, indicating that the dominant slip mode at strain of 0.05 is basal ⟨*a*⟩ slip and/or pyramidal II ⟨*c*+*a*⟩ slip. Similarly, for a strain of 0.1, all the grains with an IGMA distribution concentrated on the ⟨*uvt*0⟩ axis are shown in Fig. 8(b_1), indicating that a large number of pyramidal II ⟨*c*+*a*⟩ slips were activated. However, as shown in Fig. 8(c_1), a uniform IGMA distribution is observed in Grain C, which may be attributed to the simultaneous activation of multiple slip systems, including pyramidal ⟨*a*⟩ slip or pyramidal II ⟨*c*+*a*⟩ slip [18]. At strains of 0.5 and 0.8, the IGMA distributions of most grains are concentrated on ⟨*uvt*0⟩ axis, indicating that the dominant slip mode is pyramidal II ⟨*c*+*a*⟩ slip.

4.2.2 Schmid factor

The Schmid factor (SF, F_S) distributions of various slip systems during deformation at different strains are shown in Fig. 9. An average Schmidt factor (ASF) greater than 0.3 indicates that slip systems are more likely to be activated. Based on these criteria, at a strain of 0.05, the basal ⟨*a*⟩, pyramidal ⟨*a*⟩, and ⟨*c*+*a*⟩ slips were simultaneously activated. Nevertheless, at the middle stage of deformation (0.1, 0.2 and 0.5), the ⟨*a*⟩ slip mode was difficult to activate; thus, the ⟨*c*+*a*⟩ slip mode became dominant. Notably, at the final stage of deformation (0.8), the ⟨*a*⟩ and ⟨*c*+*a*⟩ slip modes were activated again. On the one hand, ⟨*c*⟩ dislocations cannot exist alone, and the activation of ⟨*c*+*a*⟩ dislocations consumes a large number of ⟨*a*⟩ dislocations, making them difficult to initialize. On the other hand, much energy was preferentially used for the activation of pyramidal ⟨*c*+*a*⟩ slip, and the energy allocated to ⟨*a*⟩ slip was extremely low, leading to lower activities of ⟨*a*⟩ slip. Furthermore, it is noteworthy that the impact of ⟨*c*+*a*⟩ slip does not suffice to supplant the intrinsic influence of ⟨*a*⟩ slip, thereby resulting in high dislocation density-induced stress to harmonize with strain incompatibility, consequently yielding supplementary strain hardening. Interestingly, pyramidal ⟨*c*+*a*⟩ slip manifested its activation throughout the entirety of the hot compression procedure. First, although the compression test is performed at 225 °C, a high strain rate of 30 s^{-1} favors the generation of frictional heat, thereby reducing the CRSS of non-basal slip to a certain degree [21]. Second, the pyramidal ⟨*c*+*a*⟩ slip could simultaneously modify the strain on both the *c* and a axes, which is beneficial for homogeneous deformation. Note that prismatic ⟨*a*⟩ slip with a low ASF is still difficult to initiate, which is possibly related to the original grain orientation, with the *c*-axis parallel to the CD [22].

4.2.3 CRSS calculation

Assuming uniform micro-stress acting upon each grain equivalent to the macro stress, one can derive the resolved shear stresses (τ) for various slip modes within each grain using the equation of $\tau=\sigma F_S$, wherein σ denotes the applied macro-stress. In accordance with this postulate, the distribution of τ values for diverse slip modes at strains of 0.05, 0.2, 0.5, and 0.8 is delineated in Fig. 10. Adhering to the criterion of minimal resolved shear stress, the critical resolved shear stress (CRSS) values pertaining to the distinct slip modes can be ascertained. Furthermore, the CRSS ratios associated with each slip mode are computed and presented in Table 2. The CRSS ratio between non-basal and basal ⟨*a*⟩ slip during compression reflects the activation degree of the non-basal slip mode. Table 2 shows that the value of $CRSS_{pyramidal\langle c+a\rangle}$/

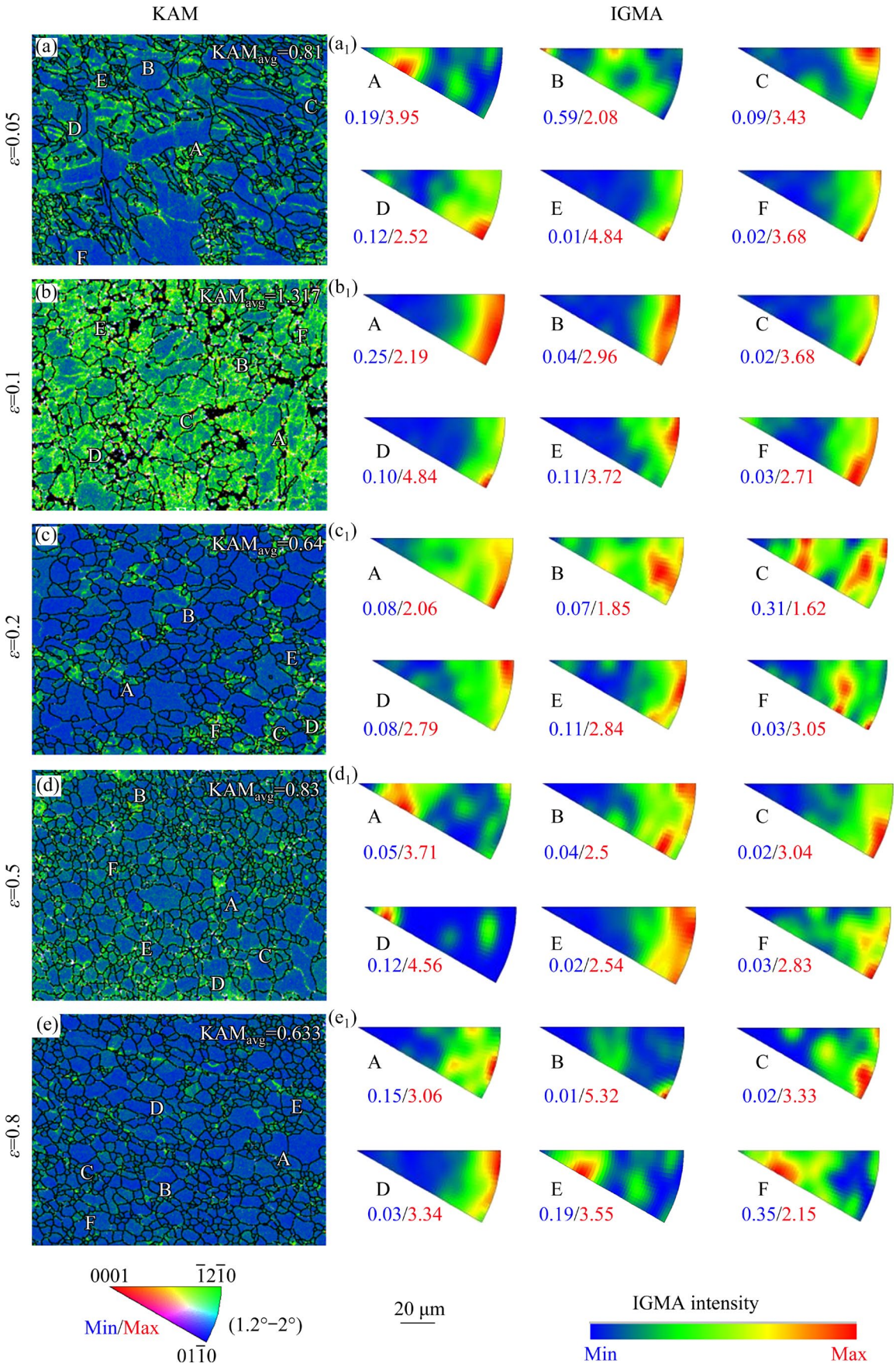

Fig. 8 KAM maps (a−e) and IGMA distribution (a_1−e_1) of BTM000 alloy obtained at different strains

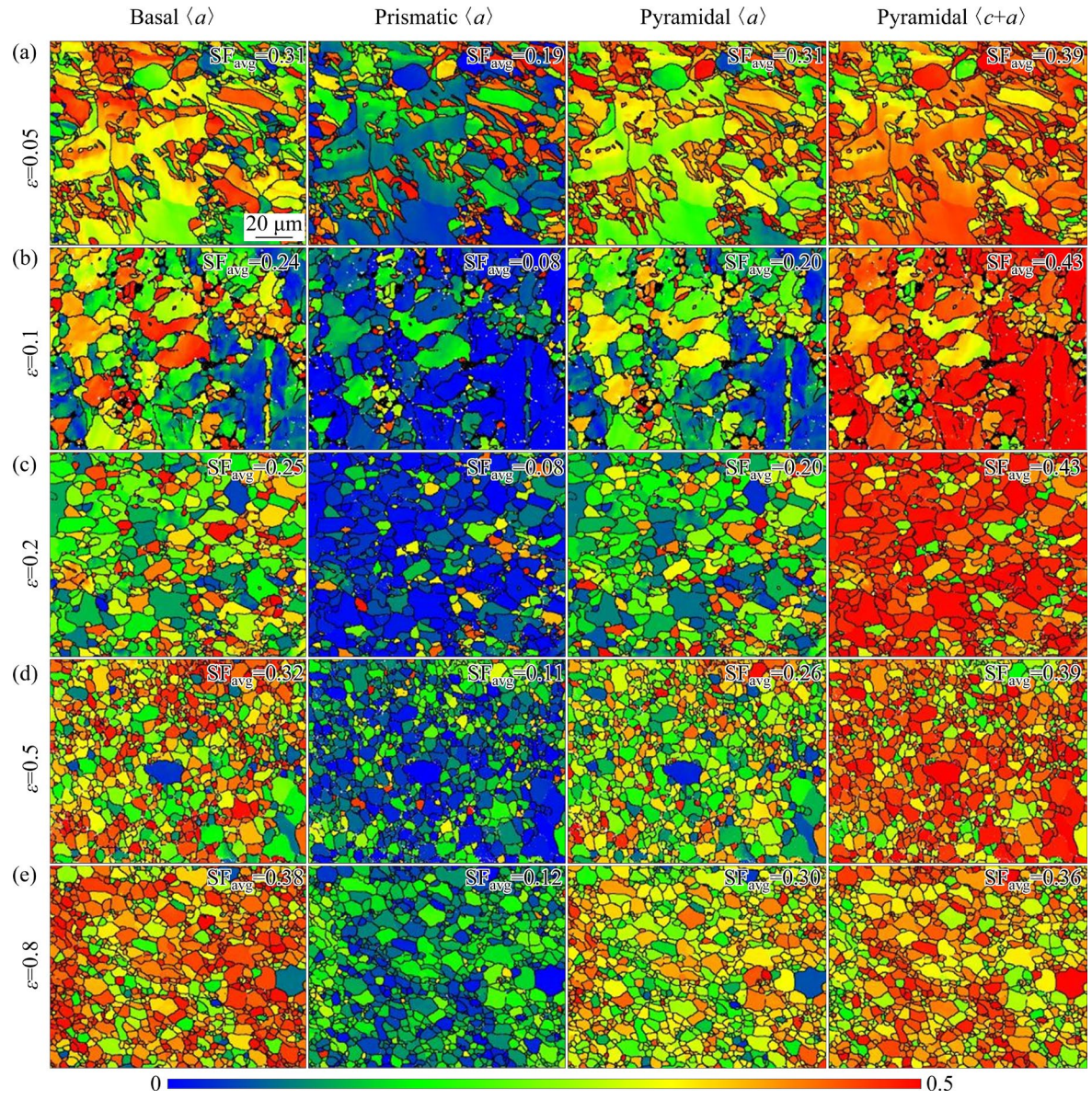

Fig. 9 Schmid factors of different slip modes

$CRSS_{basal\langle a\rangle}$ clearly declines in comparison to that of $CRSS_{pyramidal\langle a\rangle}/CRSS_{basal\langle a\rangle}$ and $CRSS_{prismatic\langle a\rangle}/CRSS_{basal\langle a\rangle}$ from strains of 0.05(31) to 0.8(6.2). This phenomenon indicates that pyramidal ⟨*c*+*a*⟩ slip is more easily activated with increasing strain, which can enhance the efficiency of DRV. The cross slip and climbing of non-basal dislocations led to dislocation rearrangement, the formation of LAGBs at the original GBs, and the absorption of new dislocations to transform into HAGBs, which subsequently formed new grains. On the other hand, the activated pyramidal ⟨*c*+*a*⟩ slip can transform the typical extrusion texture into a compression texture. In general, the grains tend to rotate perpendicular to the slip plane in the activated slip mode, resulting in texture modification during the compression process.

4.2.4 TEM identification

The bright-field TEM images at different strains are shown in Fig. 11. The invisibility criterion of $g\cdot b=0$, where g and b represent the diffraction vector and magnitude of Burgers vector, respectively, is used to analyze the dislocations [23]. The ⟨*a*⟩ and ⟨*c*+*a*⟩ dislocations are shown in Table 3.

Figures 11(a) and (b) show bright-field TEM images of the sample with a strain of 0.05 under $g=[0001]$ and $g=[10\bar{1}0]$, respectively. Many dislocation traces under $g=[0001]$ were observed, indicating that the ⟨*c*+*a*⟩ dislocations were activated. Only a few dislocations can be observed at $g=[10\bar{1}0]$.

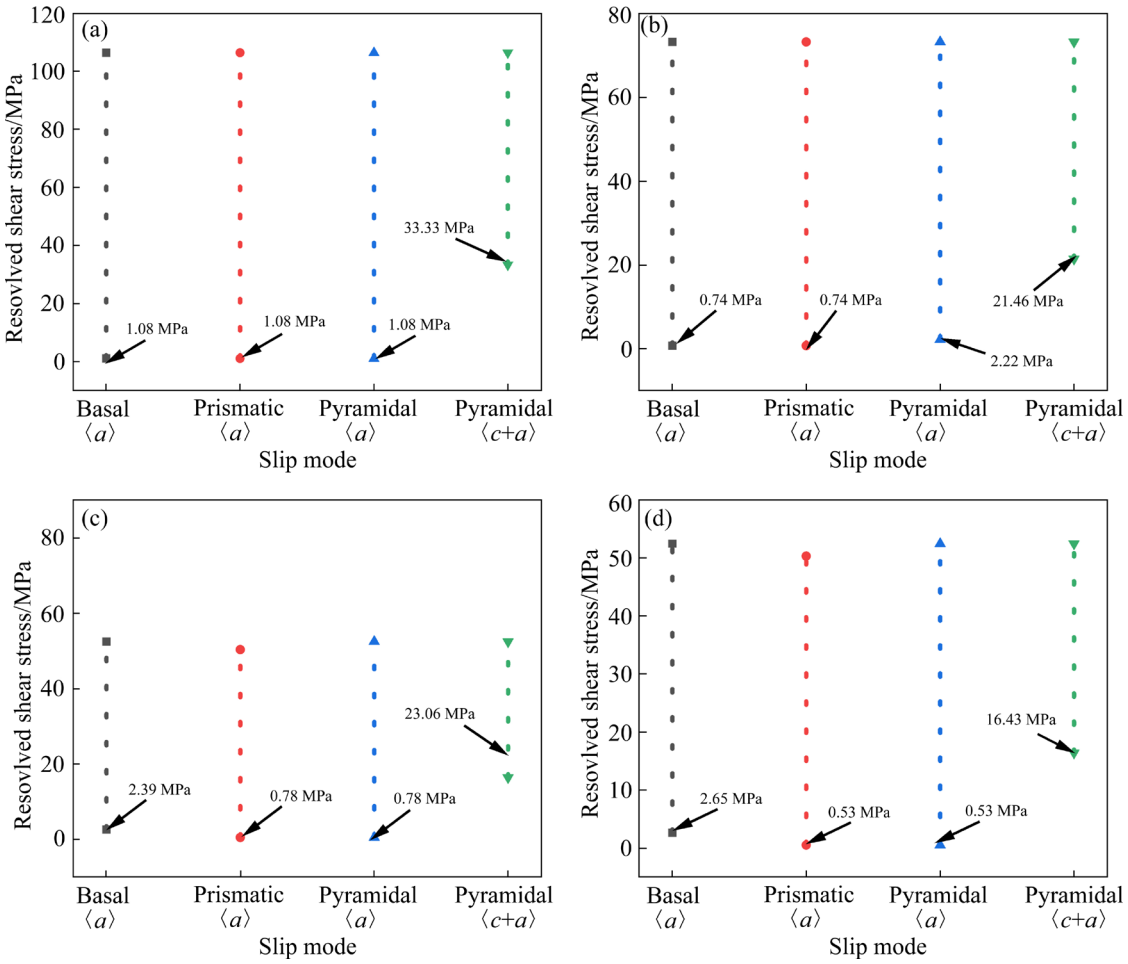

Fig. 10 Shear stresses of different slip modes of BTM000 alloy under various strains: (a) 0.05; (b) 0.2; (c) 0.5; (d) 0.8

Table 2 Calculated CRSS ratio of different slip modes in BTM000 alloy

Strain	$CRSS_{prismatic\langle a\rangle}/CRSS_{basal\langle a\rangle}$	$CRSS_{pyramidal\langle a\rangle}/CRSS_{basal\langle a\rangle}$	$CRSS_{pyramidal\langle c+a\rangle}/CRSS_{basal\langle a\rangle}$
0.05	1	3	31
0.2	1	1	29
0.5	0.33	0.33	9.65
0.8	0.2	0.2	6.2

These short dislocation segments parallel to the (0001) plane could be confirmed as basal ⟨*a*⟩ screw dislocations (marked by blue arrows, Fig. 11(c)) since *b* ($[\bar{1}2\bar{1}0]$ or $[11\bar{2}0]$) is parallel to the basal ⟨*a*⟩ dislocation lines (Fig. 11(d)). Furthermore, non-⟨*a*⟩ extended linear dislocations are discerned at the crystallographic direction *g*=[0001], as illustrated in Fig. 11(c), which is orthogonal to the (0002) plane. When considering the orientation g=$[10\bar{1}0]$, aside from the extended linear pyramidal ⟨*c*+*a*⟩ edge dislocation lines (depicted in Fig. 11(c) via green arrows), there are also some abbreviated dislocation segments that exhibit an inclination between the dislocation lines and the (0002) plane, as indicated by purple arrows in Fig. 11(c). These dislocation segments are recognized as pyramidal ⟨*a*⟩ mixed dislocations.

At a strain of 0.2, a large number of long straight pyramidal ⟨*c*+*a*⟩ edge dislocation lines could be observed, validating the activation of the ⟨*c*+*a*⟩ slip mode. Unlike in the case of 0.05, only a few basal ⟨*a*⟩ screw dislocation lines were observed. This phenomenon implies that both basal and non-basal ⟨*a*⟩ slip modes were difficult to activate, which is consistent with the results in Section 4.2.1.

4.3 DRX mechanism

The DRX nucleation mechanism is closely related to the plastic deformation mechanism. Hence, it becomes imperative to investigate the ramifications of the chosen slip mode on DRX behavior. It has been reported that the activation of ⟨*c*+*a*⟩ dislocations can enhance the efficiency of

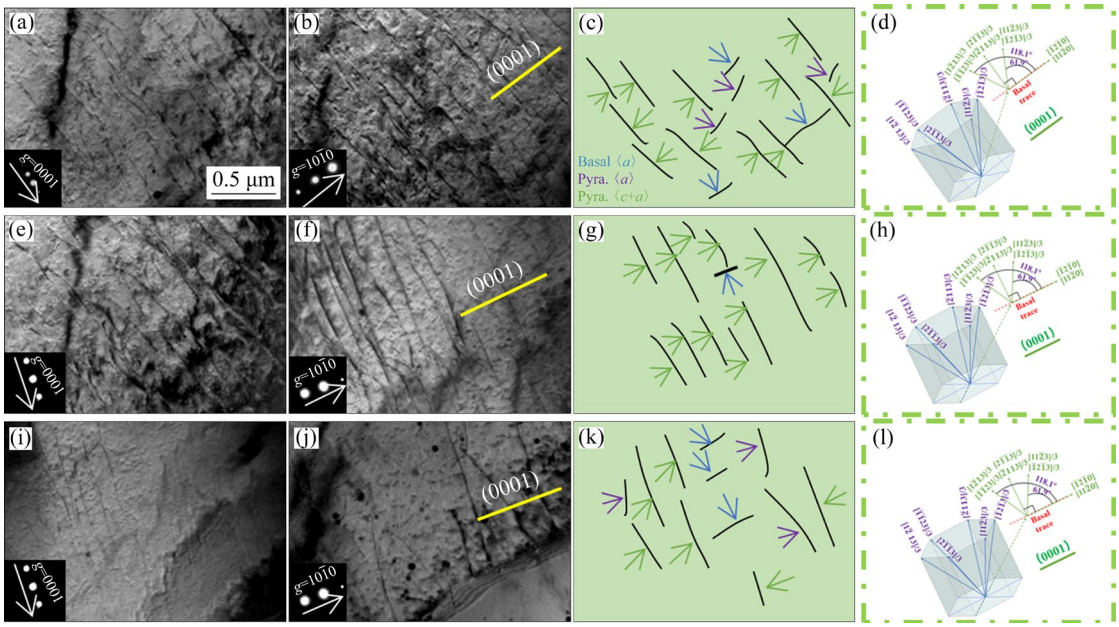

Fig. 11 TEM bright-filed images of hot compression sample subjected to different strains using two-beam diffraction including g=[0001] (a, e, i) and g=[10$\bar{1}$0] (b, f, j), and schematic diagram of slip traces of different slip modes (c, g, k) and corresponding crystal direction and plane (d, h, l): (a−d) 0.05; (e−h) 0.2; (i−l) 0.8

Table 3 Values of $g \cdot b$ at diffraction vectors used for analysis of dislocation types [24]

g	b								
	⟨a⟩			⟨c+a⟩					
	[11$\bar{2}$0]	[$\bar{1}$2$\bar{1}$0]	[$\bar{2}$110]	[11$\bar{2}$3]	[$\bar{1}$2$\bar{1}$3]	[$\bar{2}$113]	[11$\bar{2}\bar{3}$]	[$\bar{1}$2$\bar{1}\bar{3}$]	[$\bar{2}\bar{1}\bar{1}\bar{3}$]
[0002]	0	0	0	2	2	2	−2	−2	−2
[01$\bar{1}$0]	1	1	0	1	1	0	1	1	0

DRV, thereby fostering the onset of CDRX [25]. Figure 12 shows magnified IPF maps at varying strain levels. Specifically, Figs. 12(a−d) present localized enlarged IPF maps at strains of 0.1, 0.2, 0.5 and 0.8, correspondingly. As previously noted, solely the ⟨c+a⟩ slip mode was engaged at strains of 0.1, 0.2 and 0.5, while both ⟨a⟩ and ⟨c+a⟩ slip modes were concomitantly activated at a strain of 0.8.

As indicated, most of the DRXed grains are formed along the GBs of the deformed grains (Figs. 12(a−c)), which is characteristic of the DDRX mechanism [26]. Moreover, from the corresponding three-dimensional (3D) crystal orientation diagram, due to the preferential growth of DRXed grains, the newly formed DDRXed grains have orientations similar to those of the original grains, indicating that the DDRX mechanism can strengthen the texture intensity. This phenomenon was also observed in Ref. [27].

In a general context, CDRX can be ascertained by applying the criterion that the misorientation angles from the reference point exceed 15° [28]. Figures 12(e−g) illustrate magnified inverse pole figure (IPF) maps at strains of 0.1, 0.2 and 0.5, while the associated orientation gradients along lines L1, L2 and L3 are delineated in Figs. 12(g−j). From the corresponding misorientation distribution, it can be deduced that the orientation increase from point to origin exceeds 15°, indicating the occurrence of CDRX. Notably, the 3D crystal orientation diagram shows that the CDRXed grains exhibit a relatively random orientation, indicating that the CDRX process can modify the texture.

The KAM map is representative of the local deformation degree. As shown in Fig. 8(e), the average KAM value obviously decreases at strain of 0.8. This phenomenon is ascribed to the simultaneous activation of the ⟨a⟩ and ⟨c+a⟩ multiple slip systems being conducive to coordinating the deformation

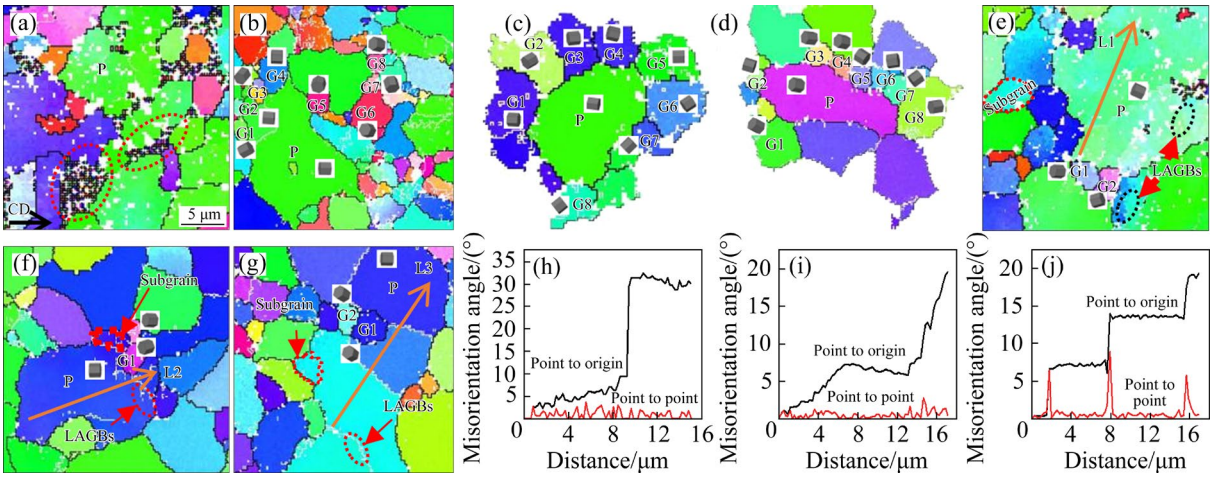

Fig. 12 High-magnification IPF maps of BTM000 alloy obtained after hot compression at different strains: (a, e) 0.1; (b, f) 0.2; (c, g) 0.5; (d) 0.8; (h–j) Orientation gradients along lines L1, L2 and L3, respectively

and thus leading to a decrease in the local storage strain. Note that only the DDRX mode and not the CDRX mode could be observed. In this respect, it is easily deduced that the required driving force (local storage strain) for DDRX is lower than that for CDRX.

In summary, the activation of the ⟨*c*+*a*⟩ slip mode in the absence of the ⟨*a*⟩ slip mode was beneficial for both the DDRX and CDRX processes, and DDRX preferentially occurred when multiple slip modes were activated due to the relatively low driving force.

4.4 Flow behavior

The variation in the flow stress curve reflects the different slip modes and twinning behaviors at different strains. In this study, at Stage I (0.05), the slight decrease in the flow stress is the result of the consumption of stress during twin nucleation. In addition, the activation of basal ⟨*a*⟩ and pyramidal ⟨*c*+*a*⟩ slip and the proliferation and entanglement of the two types of dislocations lead to a subsequent sharp increase in stress in the curve.

During Stage II (0.1), despite the twin's minimal impact on strain, it exerts a negative influence on stress contribution. Therefore, the continuous increase in flow stress is the result of the significant decrease in the twin-cell volume fraction from 16.5% to 0.767%. Interestingly, the slope of the flow curve decreases, which is mainly related to the dominant slip mode transition. From the results of TEM and SF, ⟨*a*⟩ slip is difficult to activate, and ⟨*c*+*a*⟩ slip becomes dominant at this stage. The absence of ⟨*a*⟩ slip results in a decrease in the dislocation density, which slows the work hardening rate. On the other hand, the beginning of the DRV could also lead to a decrease in the flow stress due to the decreased rate of dislocation proliferation caused by the annihilation of dislocations. Therefore, the KAM decreases from 1.317 to 0.647.

At Stage III (0.2 and 0.5), after the stress reaches its peak, the continuous decrease in the stress is the softening effect of the DRX process. With increasing dislocation density, the strain storage energy gradually reaches the critical DRX value, and DRX leads to a decrease in the flow stress. Notably, the wavy flow curve may be related to the redeformation of preferentially formed DRXed grains and the softening effect of the newly formed DRXed grains. DRX is not an instantaneous process; preferentially formed DRXed grains participate in subsequent deformation, and strain hardening leads to an increase in stress. On the other hand, the newly formed DRXed grains will consume the dislocations, resulting in a decrease in the flow stress. However, as the DRX process proceeds, the DRX degree tends to saturate, and the dislocation density decreases, which corresponds to the decreased fluctuation degree in the subsequent curve at this stage. Notably, the KAM increases again to 0.830 at a strain of 0.5, which may be related to the additional strain hardening provided by the HDI stress.

At Stage IV (0.8), the flow curve remains in dynamic equilibrium due to the softening effect of DRX and the work hardening effect. Moreover, according to the TEM analysis, the basal ⟨*a*⟩ slip was activated again. Moreover, only DDRX can be observed at this stage. Therefore, the coactivation of ⟨*a*⟩ and ⟨*c*+*a*⟩ slip may be conducive to DDRX.

4.5 HDI strain hardening

In this work, we choose the strain of 0.1 for detailed discussion, and the conditions of the other strains are similar to those in this case. Figure 13 presents strain contour maps alongside the corresponding localized enlarged IPF maps (enclosed within white rectangles) for the BTM000 alloy. Table 4 provides the computed SF values for different slip modes within the selected grains A−C. In the strain contour maps, the color red signifies pronounced local strain, whereas blue denotes minimal local strain. We select the local microregion in the red region for SF calculations to reveal the occurrence of high HDI strain hardening at strains of 0.1, 0.2, and 0.5. The above SF analysis results clearly reveal that the ASFs of basal ⟨*a*⟩ slip, prismatic ⟨*a*⟩ slip, pyramidal ⟨*a*⟩ slip and pyramidal ⟨*c*+*a*⟩ slip are 0.24, 0.08, 0.20, and 0.43, respectively. This observation suggests that the activation of pyramidal ⟨*c*+*a*⟩ slip predominated. Furthermore, as indicated in Table 3, a notable SFD discrepancy between pyramidal ⟨*c*+*a*⟩ slip (0.44, 0.12) and pyramidal ⟨*a*⟩ slip (0.13, 0.47) between grains A and B leads to localized strain concentration. Interestingly, although the SF values of grains B and C are similar, severe local strain is also observed in the regions between grains B and C, which is related to another parameter, *m*′.

The *m*′ is a crucial indicator for evaluating the deformation compatibility between neighboring grains [29,30] and is expressed as follows:

$$m'=\cos\alpha\cdot\cos\beta \tag{1}$$

where α and β are the normal angle between the slip planes and the angle between the slip directions of the adjacent grains, respectively. When *m*′ is equal to 1, the deformation compatibility is excellent. In contrast, the deformation compatibility is poor when *m*′ is 0. The m′ value of pyramidal ⟨*c*+*a*⟩ slip between grains B and C is 0.0009. Such a low value means that the deformation compatibility between grains B and C is poor. In this way, geometrically necessary dislocations (GNDs) are easily generated to accommodate the deformation incompatibility, and the accumulation of GNDs is conducive to generating higher HDI strain hardening [26].

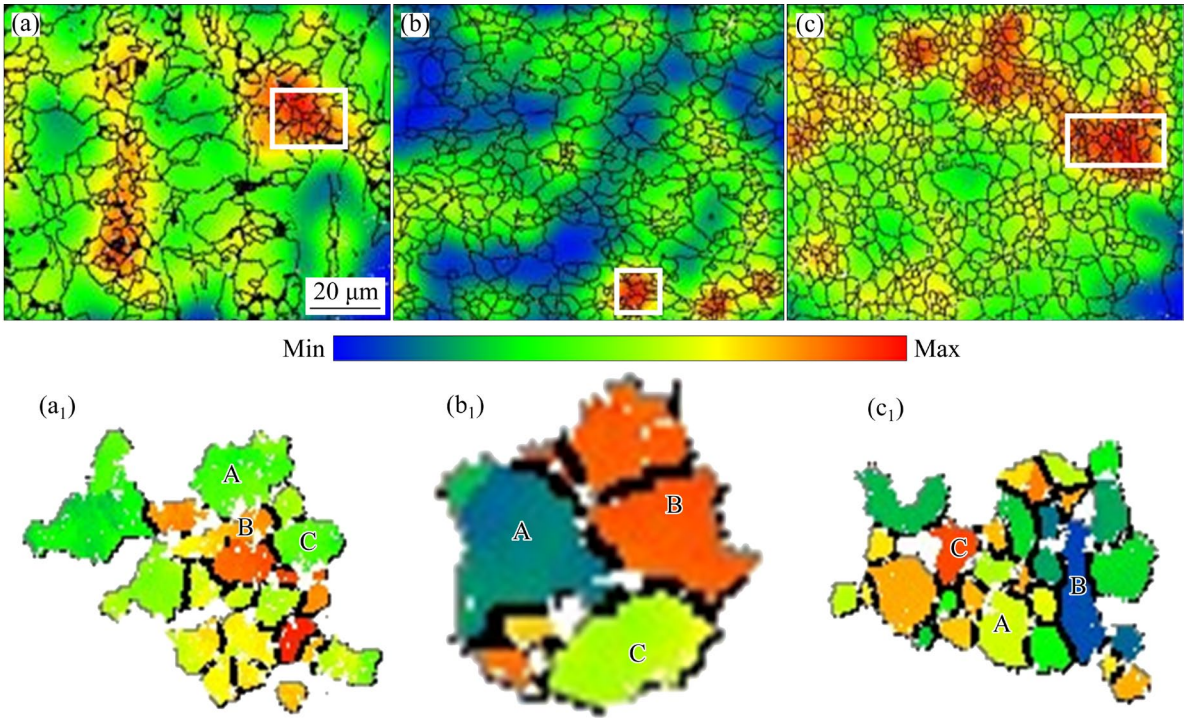

Fig. 13 Strain contouring maps (a−c) and corresponding local enlarged IPF maps (a_1−c_1) of BTM000 alloy: (a, a_1) 0.1; (b, b_1) 0.2; (c, c_1) 0.5

Table 4 Calculated SF values of different slip modes in Grains A−C

Strain	Slip mode	SF		
		Grain A	Grain B	Grain C
0.1	Basal ⟨*a*⟩ slip	0.119	0.227	0.18
	Prismatic ⟨*a*⟩ slip	0.058	0.2	0.077
	Pyramidal ⟨*a*⟩ slip	0.13	0.47	0.221
	Pyramidal ⟨*c*+*a*⟩ slip	0.44	0.12	0.4
0.5	Basal ⟨*a*⟩ slip	0.23	0.078	0.26
	Prismatic ⟨*a*⟩ slip	0.03	0.002	0.1
	Pyramidal ⟨*a*⟩ slip	0.17	0.048	0.21
	Pyramidal ⟨*c*+*a*⟩ slip	0.47	0.5	0.39

5 Conclusions

(1) At a modest strain level of 0.05, both basal ⟨*a*⟩ slip and pyramidal ⟨*a*⟩ and ⟨*c*+*a*⟩ slip modes were concurrently initiated. Nevertheless, at the middle stage of deformation (0.1, 0.2, and 0.5), ⟨*a*⟩ slip modes were difficult to activate; thus, the ⟨*c*+*a*⟩ slip mode became dominant. Finally, in addition to ⟨*c*+*a*⟩, the basal ⟨*a*⟩ slip mode was activated again at a strain of 0.8.

(2) Since the ⟨*c*+*a*⟩ slip mode was insufficient to replace the inherent effect of the ⟨*a*⟩ slip mode, heterodeformation-induced (HDI) stress was generated to provide additional strain hardening. Furthermore, the lower compatibility factor (m') between adjacent grains in the microdomain was conducive to generating higher HDI strain hardening.

(3) The value of $CRSS_{pyramidal\langle c+a\rangle}/CRSS_{basal\langle a\rangle}$ decreased more evidently than did that of $CRSS_{pyramidal\langle a\rangle}/CRSS_{basal\langle a\rangle}$ and $CRSS_{prismatic\langle a\rangle}/CRSS_{basal\langle a\rangle}$ from a strain of 0.05 (31) to 0.8 (6.2).

(4) The softening effect related to CDRX and DDRX dominated the deformation process at strains ranging from 0.2 to 0.5. Furthermore, the initiation of the ⟨*c*+*a*⟩ slip mode in the absence of the ⟨*a*⟩ slip mode proved advantageous for the onset of CDRX. Conversely, at a strain level of 0.8, the simultaneous activation of both ⟨*c*+*a*⟩ and basal ⟨*a*⟩ slip modes led to DDRX as the sole DRX mode.

CRediT authorship contribution statement

Zhi-yong YOU: Conceptualization, Investigation, Formal analysis, Writing − Original draft, Writing − Review & editing; **Wei-li CHENG:** Conceptualization, Supervision, Project administration, Writing − Review & editing; **Guo-lei LIU:** Validation, Formal analysis, Writing − Review & editing; **Jian LI:** Funding acquisition, Resources; **Li-fei WANG:** Methodology, Writing − Review & editing; **Hui YU:** Formal analysis, Writing − Review & editing; **Hong-xia WANG:** Supervision; **Ze-qin CUI:** Supervision; **Jin-hui WANG:** Supervision.

Declaration of competing interest

The authors declare that they have no known competing financial interests or personal relationships that could have appeared to influence the work reported in this paper.

Acknowledgments

This work was supported by the National Natural Science Foundation of China (No. 51901153), Shanxi Scholarship Council of China (No. 2019032), Natural Science Foundation of Shanxi Province, China (No. 202103021224049), the Shanxi Zhejiang University New Materials and Chemical Research Institute Scientific Research Project, China (No. 2022SX-TD025), and the Open Project of Salt Lake Chemical Engineering Research Complex, Qinghai University, China (No. 2023-DXSSKF-Z02).

References

[1] SANDLÖBES S, ZAEFFERER S, SCHESTAKOW I, YI S, GONZALEZ-MARTINEZ R. On the role of non-basal deformation mechanisms for the ductility of Mg and Mg–Y alloys [J]. Acta Materialia, 2011, 59: 429−439.

[2] HADORN J P, HANTZSCHE K, YI S B, BOHLEN J, LETZIG D, WOLLMERSHAUSER J A, AGNEW S R. Role of solute in the texture modification during hot deformation of Mg-rare earth alloys [J]. Metallurgical and Materials Transactions A, 2012, 43: 1347−1362.

[3] KIM K H, JEON J B, KIM N J, LEE B J. Role of yttrium in activation of ⟨*c*+*a*⟩ slip in magnesium: An atomistic approach [J]. Scripta Materialia, 2015, 108: 104−108.

[4] JANG H S, LEE B J, Effects of Zn on ⟨*c*+*a*⟩ slip and grain boundary segregation of Mg alloys [J]. Scripta Materialia, 2019, 160: 39−43.

[5] SHEN Jing-yuan, ZHANG Ling-yu, HU Lian-xi, SUN Yu, GAO Fei, LIU Wen-chao, YU Huan. Effect of subgrain and the associated DRX behaviour on the texture modification of Mg−6.63Zn−0.56Zr alloy during hot tensile deformation [J]. Materials Science and Engineering A, 2021, 823: 141745.

[6] YASI J A, HECTOR L G, TRINKLE D R. First-principles data for solid-solution strengthening of magnesium: From geometry and chemistry to properties [J]. Acta Materialia, 2010, 58: 5704−5713.

[7] CHAUDRY U M, KIM T H, PARK S D, KIM Y S, HAMAD

K, KIM J G. Effects of calcium on the activity of slip systems in AZ31 magnesium alloy [J]. Materials Science and Engineering A, 2019, 739: 289−294.

[8] WU Qin, YAN Hong-ge, CHEN Ji-hua, XIA Wei-jun, SONG Ming, SU Bin. Dynamic precipitation behavior before dynamic recrystallization in a Mg−Zn−Mn alloy during hot compression [J]. Materials Characterization, 2019, 153: 14−23.

[9] WU Xiao-lei, YANG Mu-xin, YUAN Fu-ping, WU Gui-lin, WEI Yu-jie, HUANG Xiao-xu, ZHU Yun-tian. Heterogeneous lamella structure unites ultrafine-grain strength with coarse-grain ductility [J]. Proceedings of the National Academy of Sciences of the United States of America, 2015, 112: 14501−14505.

[10] ZHANG Zhi, ZHANG Jing-huai, WANG Wen-ke, LIU Shu-juan, SUN Bin, XIE Jin-shu, XIAO Ting-xu. Unveiling the deformation mechanism of highly deformable magnesium alloy with heterogeneous grains [J]. Scripta Materialia, 2022, 221: 114963.

[11] LIU Shuai-shuai, YANG Fei-xiang, YANG Hong, HUANG Guang-sheng, TANG Ai-tao, CHEN Xian-hua, JIANG Bin, PAN Fu-sheng. High-resolution mapping of the strain heterogeneity in heterogeneous and homogeneous structured Mg13Gd alloy [J]. Materials Characterization, 2022, 193: 112335.

[12] LIU Guo-lei, CHENG Wei-li, LUO Lin, YU Hui, WANG Li-fei, LI Hang, WANG Hong-xia, WANG Jin-hui. Hot compression deformation behavior and dynamic recrystallization of a precipitate-free Mg−Bi−Sn alloy [J]. Journal of Materials Research and Technology, 2023, 25: 497−510.

[13] SOMEKAWA H, SINGH A. Superior room temperature ductility of magnesium dilute binary alloy via grain boundary sliding [J]. Scripta Materialia, 2018, 150: 26−30.

[14] WANG Qing-hang, WANG Li, ZHAI Hao-wei, CHEN Yang, CHEN Shuai. Establishment of constitutive model and analysis of dynamic recrystallization kinetics of Mg−Bi−Ca alloy during hot deformation [J]. Materials, 2022, 15: 7986.

[15] GAN Yi, HU Li, SHI Lai-xin, CHEN Qiang, LI Ming-ao, XIANG Lin, ZHOU Tao. Effect of AlLi phase on deformation behavior and dynamic recrystallization of Mg−Li alloy during hot compression [J]. Transactions of Nonferrous Metals Society of China, 2023, 33: 1373−1384.

[16] ZHU Yu-long, CAO Yu, LIU Cun-jian, LUO Rui, LI Na, SHU Gang, HUANG Guang-jie, LIU Qing. Dynamic behavior and modified artificial neural network model for predicting flow stress during hot deformation of Alloy 925 [J]. Materials Today Communications, 2020, 25: 101329.

[17] GALIYEV A, KAIBYSHEV R, GOTTSTEIN G. Correlation of plastic deformation and dynamic recrystallization in magnesium alloy ZK60 [J]. Acta Materialia, 2001, 49: 1199−1207.

[18] CHEN Xiao-yang, ZHANG Yang, CONG Meng-qi, LU Ya-lin, LI Xiao-ping. Effect of Sn content on microstructure and tensile properties of as-cast and as-extruded Mg−8Li−3Al−(1,2,3)Sn alloys [J], Transactions of Nonferrous Metals Society of China, 2020, 30: 2079−2089.

[19] XU Shi-wei, ZHU Cong-cong, LIN Zhan-hong, JIN Chen, KAMADO S, OH-ISHI K, QIN Yun. Dynamic microstructure evolution and mechanical properties of dilute Mg−Al−Ca−Mn alloy during hot rolling [J]. Journal of Materials Science & Technology, 2022, 129: 1−14.

[20] CHUN Y B, BATTAINI M, DAVIES C H J, HWANG S K. Distribution characteristics of in-grain misorientation axes in cold-rolled commercially pure titanium and their correlation with active slip modes [J]. Metallurgical and Materials Transactions A, 2010, 41: 3473−3487.

[21] GUI Yun-wei, OUYANG Ling-xiao, XUE Yi-bei, LI Quan-an. Effect of thermo-mechanical processing parameters on the dynamic restoration mechanism in an Mg−4Y−2Nd−1Sm−0.5Zr alloy during hot compression [J]. Journal of Materials Science & Technology, 2021, 90: 205−224.

[22] FAN Ding-ge, DENG Kun-kun, WANG Cui-ju, NIE Kai-bo, SHI Ouan-xin, LIANG Wei. Hot deformation behavior and dynamic recrystallization mechanism of an Mg−5wt.%Zn alloy with trace SiC_p addition [J]. Journal of Materials Research and Technology, 2021, 10: 422−437.

[23] WU Zhao-xuan, AHMAD R, YIN Bing-lun, SANDLÖBES S, CURTIN W A. Mechanistic origin and prediction of enhanced ductility in magnesium alloys [J]. Science, 2018, 359: 447−452.

[24] CHEN Yang, WANG Qing-hang, WANG Li, ZHAI Hao-wei, HUANG Li-xin, JIANG Bin, MAO Yong, HE Jun-jie. Deformation mechanisms of as-extruded Mg−3Bi−1Ca (wt.%) alloy during room-temperature tension [J]. Materials Science and Engineering A, 2023, 875: 145119.

[25] DENG Ying, ZHU Xin-wen, LAI Yi, GUO Yi-fan, FU Le, XU Guo-fu, HUANG Ji-wu. Effects of Zr/(Sc+Zr) microalloying on dynamic recrystallization, dislocation density and hot workability of Al−Mg alloys during hot compression deformation [J]. Transactions of Nonferrous Metals Society of China, 2023, 33: 668−682.

[26] SAKAI T, MIURA H, GOLOBORODKO A, SITDIKOV O. Continuous dynamic recrystallization during the transient severe deformation of aluminum alloy 7475 [J]. Acta Materialia, 2009, 57: 153−162.

[27] ZHANG Yu-qin, CHENG Wei-li, YU Hui, WANG Hong-xia, NIU Xiao-feng, WANG Li-fei, LI Hang. Unveiling the twinning and dynamic recrystallization behavior and the resultant texture evolution in the extruded Mg−Bi binary alloys during hot compression [J]. Journal of Materials Science & Technology, 2022, 105: 274−285.

[28] LIN Y C, HE Dao-guang, CHEN Ming-song, CHEN Xiao-min, ZHAO Chun-yang, MA Xiang, LONG Zhi-li. EBSD analysis of evolution of dynamic recrystallization grains and δ phase in a nickel-based superalloy during hot compressive deformation [J]. Materials & Design, 2016, 97: 13−24.

[29] SHI Zhang-zhi, LIU Xue-feng. Characteristics of cross grain boundary contraction twin pairs and bands in a deformed Mg alloy [J]. Journal of Alloys and Compounds, 2017, 692: 274−279.

[30] LV Bin-jiang, WANG Sen, CUI Ning, GUO Feng. Twinning and dynamic recrystallization of Mg−7Sn−3Zn alloy under high strain rate hot compression [J]. Materials Science and Engineering A, 2021, 809: 140986.

⟨*c*+*a*⟩滑移模式对挤压态低合金化 Mg−0.5Bi−0.5Sn−0.5Mn 合金显微组织演变和压缩流变行为的影响

游志勇[1]，程伟丽[1,2]，刘国磊[1]，李 戬[2]，王利飞[1]，余 晖[3]，王红霞[1]，崔泽琴[1]，王金辉[2]

1. 太原理工大学 材料科学与工程学院，太原 030024；
2. 青海大学 部省合建盐湖化工大型系列研究设施，西宁 810016；
3. 河北工业大学 材料科学与工程学院，天津 300132

摘 要：通过电子背散射衍射、X 射线衍射、透射电子显微分析和热压缩实验，深入分析滑移模式对挤压态低合金化 Mg−0.5Bi−0.5Sn−0.5Mn 合金显微组织演变和不同应变下压缩流变行为的影响。结果表明，在 0.05 的低应变下，基面⟨*a*⟩、锥面⟨*a*⟩和⟨*c*+*a*⟩滑移模式同时被激活。然而，在变形中期阶段(应变 0.1、0.2 和 0.5)，⟨*a*⟩滑移模式很难被激活，因此，⟨*c*+*a*⟩滑移模式占主导地位。此外，与连续动态再结晶和非连续动态再结晶有关的软化效应主导应变为 0.2~0.5 的变形过程。最后，在 0.8 应变阶段，由于非连续动态再结晶引起的动态软化和基面⟨*a*⟩滑移模式激活引起的加工硬化效应达到动态平衡，流变应力保持恒定。

关键词：低合金化 Mg−Bi−Sn−Mn 合金；滑移模式；热压缩；流变行为；动态再结晶

(Edited by Xiang-qun LI)